Organ-Specific Immune Setpoints Underlie Divergent Immune Profiles across Metastatic Sites in Breast Cancer

Colt A. Egelston[1], Weihua Guo[1], Diana L. Simons[1], Jian Ye[1], Christian Avalos[1], Shawn T. Solomon[1], Mary Nwangwu[1], Michael S. Nelson[2], Jiayi Tan[1], Eliza R. Bacon[3], Kena Ihle[3], Daniel Schmolze[4], Lusine Tumyan[5], James R. Waisman[3], and Peter P. Lee[1]

ABSTRACT

Immune composition within the tumor microenvironment (TME) plays a central role in the propensity of cancer cells to metastasize and respond to therapy. Previous studies have suggested that the metastatic TME is immune-suppressed. However, limited accessibility to multiple metastatic sites within patients has made assessing the immune TME difficult in the context of multiorgan metastases. We utilized a rapid postmortem tissue collection protocol to assess the immune composition of numerous sites of breast cancer metastasis and paired tumor-free tissues. Metastases had comparable immune cell densities and compositions to paired tumor-free tissues of the same organ type. In contrast, immune cell densities in both metastatic and tumor-free tissues differed significantly between organ types, with lung immune infiltration being consistently greater than that in the liver. These immune profiling results were consistent between flow cytometry and multiplex immunofluorescence–based spatial analysis. Furthermore, we found that granulocytes were the predominant tumor-infiltrating immune cells in lung and liver metastases, and these granulocytes comprised most PD–L1–expressing cells in many tissue sites. We also identified distinct potential mechanisms of immunosuppression in lung and liver metastases, with the lung having increased expression of PD-L1$^+$ antigen-presenting cells and the liver having higher numbers of activated regulatory T cells and HLA-DR^{low} monocytes. Together, these results demonstrate that the immune contexture of metastases is dictated by organ type and that immunotherapy strategies may benefit from unique tailoring to the tissue-specific features of the immune TME.

Introduction

Nearly one in three women with breast cancer will develop metastatic breast cancer (MBC) at a later time (1). Despite the recent rapid evolution of treatment options for these patients, MBC is still considered incurable (2). Response rates to immune checkpoint inhibitors (ICI) in most patients with MBC are low, with rare survival benefit mainly in triple-negative (TN) patients with MBC with high levels of PD-L1 expression (3). Consequently, therapeutics for TN MBC and hormone receptor-positive (HR+) patients with MBC are still centered on chemotherapy and endocrine therapy backbones, respectively. A comprehensive characterization of immune composition in the MBC tumor microenvironment (TME) is currently lacking. Improving clinical responses to immunotherapy in patients with MBC demands a vast improvement in our understanding of immune TME features, specifically in metastasis (4, 5).

MBC disseminates to multiple distant organs, including lung, liver, bone marrow, brain, and skin (6). In general, evidence suggests that the metastatic TME harbors features of immune escape (7–10). However, immune profiling studies of metastatic TME have been hampered by interpatient heterogeneity and limited biopsy accessibility at certain tissue sites. As a result, it is unclear how immune composition may vary across multifocal metastatic tumor sites. Thus, understanding how organ-specific features of metastatic sites drive response to therapy is a major challenge in current immunotherapy designs (11).

To shed light on these key unresolved questions, we interrogated the composition of immune subsets in the TME of MBC by leveraging the collection of tissues from multiple metastatic and paired tumor-free sites from nine postmortem patients. By using matched tissues collected at a single time, we could perform an unprecedented assessment of how the immune context of MBC varies by tissue site. Through robust quantification of most major immune cell phenotypes, including CD8$^+$ and CD4$^+$ T-cell subsets, B-cell subsets, NK–cell subsets, tumor-associated monocytes/macrophages, dendritic-cell (DC) subsets, and granulocyte subsets, we show that organ site of metastasis dictates the abundance and composition in the tumor immune microenvironment. Our data demonstrate that immune heterogeneity in multiorgan metastatic disease must be considered in the design of immunotherapy strategies and the interpretation of immune biomarkers from tissue biopsies.

Materials and Methods

Human samples

Tissue specimens were collected from patients with MBC who gave institutional review board (IRB) approved written informed consent before inclusion in the study (City of Hope IRB 17503). The research use of these specimens for this study was reviewed and approved by City of Hope IRB 18352 in compliance with all relevant

[1]Department of Immuno-Oncology, Beckman Research Institute, City of Hope, Duarte, California. [2]The Light Microscopy and Digital Imaging Core, Beckman Research Institute, City of Hope, Duarte, California. [3]Department of Medical Oncology, City of Hope, Duarte, California. [4]Department of Pathology, City of Hope, Duarte, California. [5]Department of Diagnostic Radiology, City of Hope, Duarte, California.

C.A. Egelston and W. Guo contributed equally to this article.

Corresponding Author: Peter P. Lee, Department of Immuno-Oncology, City of Hope Comprehensive Cancer Center, Beckman Center, Room 5117, 1500 East Duarte Road, Duarte, CA 91010. E-mail: plee@coh.org

Cancer Immunol Res 2024;XX:XX–XX

doi: 10.1158/2326-6066.CIR-23-0718

ethical regulations, including the Declaration of Helsinki. Tissue samples were provided by the City of Hope "Legacy Project" for rapid tissue donation. Our group has previously described recruitment and consenting methods in detail (12). Briefly, nine patients with MBC and their families were approached and consented to body and tissue donation, either before or at the time of death. The cause of death was largely because of organ failure, with patients 1 and 7 having lung failure, patients 2, 3, and 9 having liver failure, and patient 8 having multiorgan failure. Patients 4 and 5 expired because of hemorrhagic stroke and terminal sedation, respectively.

Patient primary tumor clinical characteristics are summarized in Supplementary Table S1 and a summary of tissue types collected is found in **Fig. 1**. For this study, specimens collected from tumor-free organs, including contralateral, or tumor-free adjacent tissues, are considered "tumor-negative." Because of limited cell numbers obtained from patient samples, not all analyses were performed on all specimens. Other investigators may have received specimens from the same patients.

Sample processing and quality control

Tissue specimens were resected and collected within 6 hours after death. Each solid tissue specimen was segmented for downstream flow cytometry and histology. For single-cell suspensions for flow cytometry, tissues were placed into tubes containing cold RPMI (Life Technologies, Thermo Fisher Scientific) and transported on ice to the laboratory for processing within 6 hours of collection. Tumor-negative and tumor-involved tissues were minced into pieces, mechanically dissociated with a gentleMACS Dissociator (Miltenyi Biotec), and enzymatically treated with 0.2 Wunsch U/mL Liberase TM (Roche) and 10 U/mL DNase (Sigma) in RPMI for up

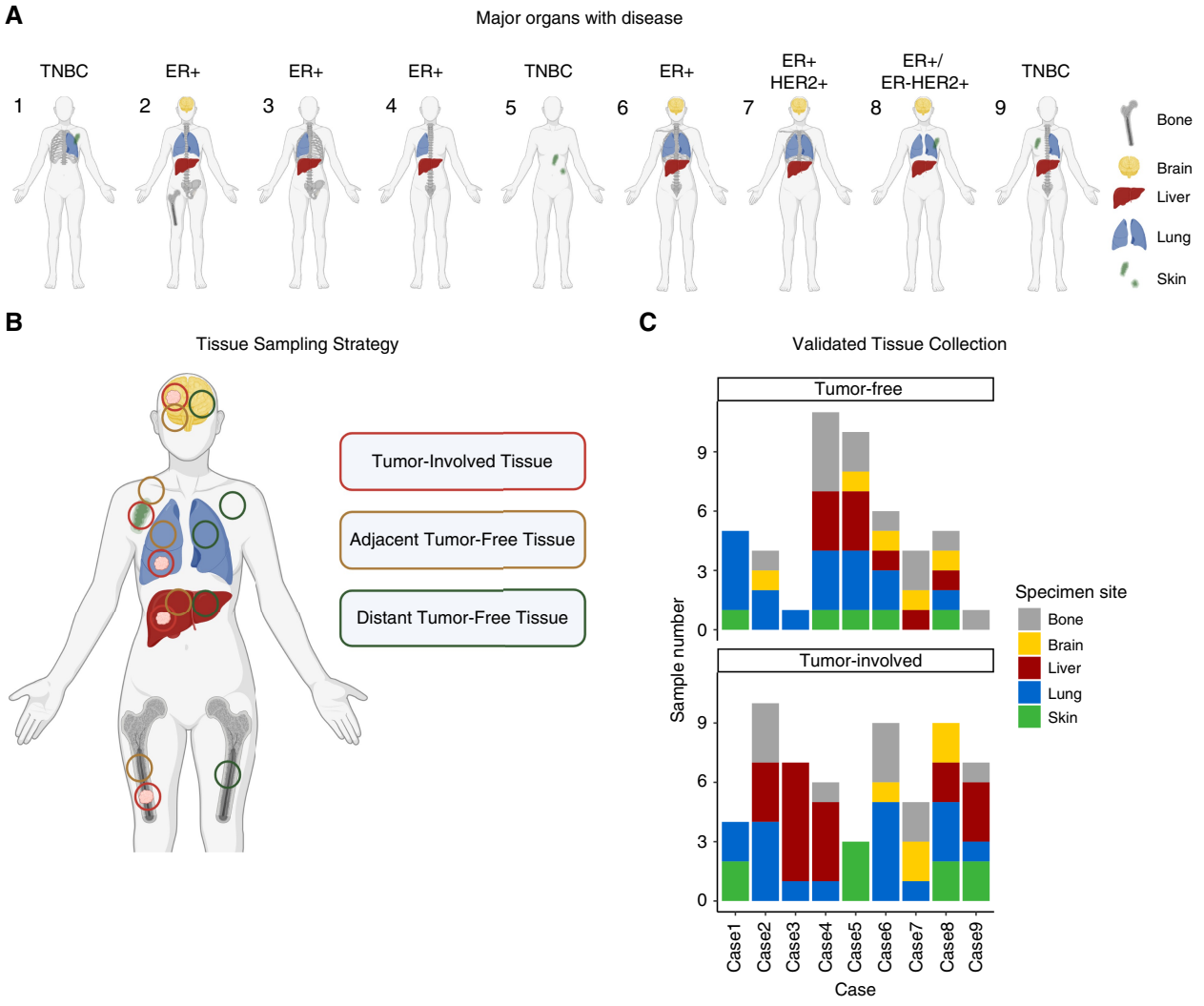

Figure 1.

Summary of postmortem tissue collection. **A,** Depiction of tumor-involved organs procured from patients and assayed for immune phenotyping. Patients are labeled by case number and whether their primary tumor was ER$^+$, HER2$^+$, or TNBC. Patient 7 had ER$^+$ and ER$^-$HER2$^+$ metachronous primary tumors. **B,** Tissue sampling strategy involved collecting grossly identified tumor-involved tissue, adjacent tumor-free tissue, and distant tumor-free tissue sites. **C,** Summary of the total number of pathologist-validated tissue specimens collected from each tumor-free or tumor-involved organ site across all patients. (Created with BioRender.com).

to 1 hour as needed. Single-cell suspensions from bone were obtained by placing a piece of bone into a 50 mL conical tube containing cold RPMI and vigorously shaking to release immune cells. If necessary, red blood cell (RBC) lysis was performed using RBC Lysis Buffer (Biolegend). For histology, tissues were fixed with 10% formalin for at least 48 hours. Tissues were then rinsed with PBS, transferred to a tissue cassette, and placed in 70% ethanol overnight. Fixed tissues were then paraffin embedded by the histology core. Histological H&E staining was performed on all specimens in a clinical pathology laboratory using standard procedures. Tissues were validated by a board-certified pathologist and scored for necrosis, tumor cellularity, and TILs. Specimens with less than 50% necrosis were used in this dataset. For hierarchical clustering in the heatmaps, specimens with more than 60% missing cell subsets were excluded in **Fig. 2C**.

Flow cytometry

Single-cell suspensions were stained with a dead cell exclusion dye Zombie Red (Biolegend) and blocked with Fc receptor blocking TruStain FcX (Biolegend) before antibody staining. Samples were stained at RT in 2% FBS (Genesee Scientific) in PBS. For cytokine production assays, cells were stimulated with 50 ng/mL PMA (Sigma) and 1 μg/mL ionomycin (Sigma) in the presence of Golgi Plug (Biolegend) for 4 hours. Fixation was performed with IC Fixation Buffer (eBioscience). Fixation and permeabilization were performed using BD Cytofix/Cytoperm buffers for intracellular cytokine staining. The antibody cocktails were diluted in Brilliant Violet Buffer (BD Biosciences). Samples were acquired using a BD Fortessa operating FACS Diva 6.1.3. Photomultiplier tube voltages were set using BD CS&T beads. Compensation was calculated using single-stained OneComp compensation beads (eBioscience). Samples were stained with fluorescently tagged antibodies detailed in Supplementary Table S2. Antibodies were titrated to determine the optimal signal-to-noise ratio before use. Flow cytometry was performed using Flowjo v10.8. All samples were gated on live single cells.

Immunohistochemistry

Formalin-fixed, paraffin-embedded (FFPE) tissue samples were sectioned at a thickness of 4 μm, baked, and placed on positively charged glass slides. Slides were loaded on a Ventana Discovery Ultra (Ventana Medical Systems, Roche Diagnostics) automated IHC staining machine for deparaffinization, rehydration, endogenous peroxidase activity inhibition, and antigen retrieval (pH 8.5). Slides were stained for estrogen receptor (ER) (clone SP1 250), PR (clone 1E2), HER2 (clone 4B5), Ki-67 (clone 30-9), and PD-L1 (clone SP263), with DISCOVERY anti-Rabbit HQ as the secondary antibody. Staining was visualized with DISCOVERY Yellow Kit or DAB, counterstained with hematoxylin (Ventana), and coverslipped. Slides were imaged at 10× magnification using the Vectra 3 Automated Quantitative Pathology Imaging System (Akoya Biosciences). Slides were scored for marker expression by a board-certified pathologist.

Multiplex immunofluorescence

FFPE tissue samples were sectioned at a thickness of 4 μm, baked, and placed on positively charged glass slides. Slides were deparaffinized in xylene and rehydrated in decreasing gradients of ethanol. Heat-mediated antigen retrieval was performed in AR6 or AR9 (Akoya Biosciences) buffer using a microwave oven. Blocking was performed using Antibody Diluent and Background Reducing (Agilent). Primary antibodies (Supplementary Table S3) were added, and slides were incubated for 1 hour at room temperature. Primary antibodies were detected using Mach 2 Rabbit or Mouse HRP-Polymer (Biocare Medical) and then labeled with fluorescent dyes using Opal Color Fluorophores (Akoya Biosciences). Cell nuclei were labeled with DAPI (Akoya Biosciences), and coverslips were mounted with ProLong Gold Antifade Mountant (Thermo Fisher Scientific).

Stained slides were imaged using the Vectra 3 Automated Quantitative Pathology Imaging System (Akoya Biosciences) to obtain images of 10× and 20× magnification. Phenochart (Akoya Biosciences) was used to visualize and annotate regions of interest. inForm Tissue Analysis Software (Akoya Biosciences) was used to unmix and export multichannel tiff images, which were then analyzed as whole slides in QuPath (13). Areas of necrosis, tissue folds, and autofluorescence were omitted from tissue analysis with the guidance of a breast cancer pathologist. Control tonsils were stained and imaged simultaneously with experimental samples to validate staining quality. Tonsil FFPE tissue samples were provided by the NCI Cooperative Human Tissue Network. Other investigators may have received specimens from the same tissue specimens.

Unsupervised clustering and dimension reduction

The densities of 34 different cell types were $\log_{10}$ transformed and scaled before clustering. The "pam" clustering algorithm, a more robust version of K-means, was implemented to identify the clusters (14). The optimal cluster number was determined by the elbow point of the total within the sum of squares and the highest value of gap statistics. Uniform manifold approximation and projection (UMAP) was implemented to reduce the dimension of 2D visualization. The cell densities of each cluster were compared with all the other clusters together, corresponding to the Wilcoxon rank sum test, to identify the markers of each cluster. Fisher's exact test was used for specimen sites and cases for the clinical features, and the Kruskal–Wallis test was used for ER, PR, HER2 score, and Ki67%.

Additional statistics

Graphs and statistics were performed using specific R packages as described. Statistics described were generated using Wilcoxon rank sum tests or Kruskal–Wallis test by ranks. Calculated P values are displayed as *, $P < 0.05$; **, $P < 0.01$; ***, $P < 0.001$; ****, $P < 0.0001$. For all graphs, the mean is represented by a horizontal line. Experiment-specific detailed statistic methods are described in corresponding figure legends and method sections.

Data availability

All data generated in the study are provided in the manuscript and are summarized graphically in supplementary data files. Any additional data generated in this study are available upon request from the corresponding author.

Results

Rapid immune profiling of tissues in patients with metastatic disease

We collected postmortem tissues from nine female patients with multifocal MBC. A summary of patient and clinical characteristics at the time of initial primary diagnosis is summarized in Supplementary Table S1. Assessment of these patients' disease progression and tumor characteristics has been reported elsewhere (15). Patient age at initial diagnosis ranged from 31 to 69, with a median age of

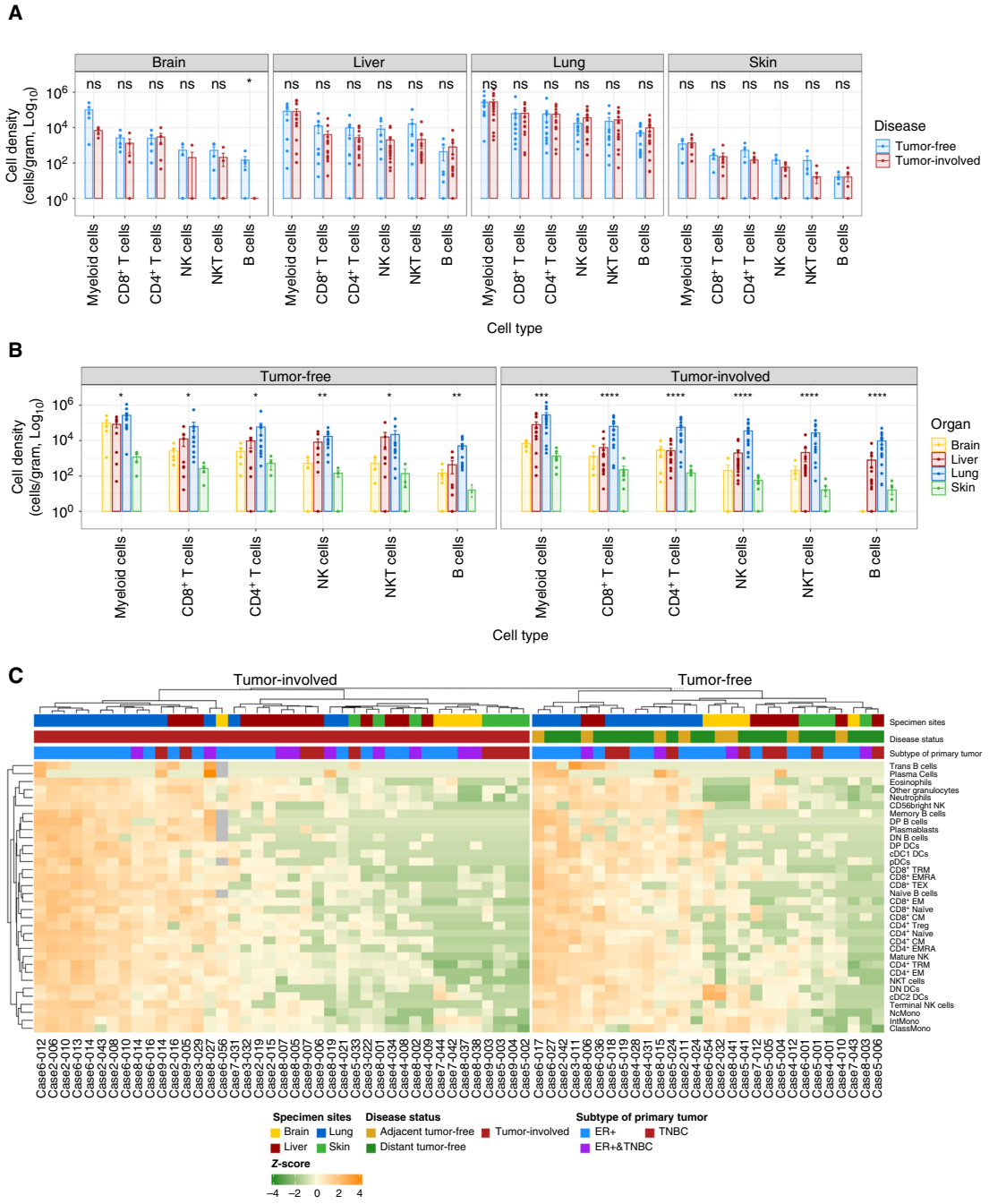

Figure 2.

Metastatic tumor immune densities are defined by organ type. **A,** Densities of myeloid cells, $CD8^+$ T cells, $CD4^+$ T cells, NK, NKT, and B cells in tumor-free (blue) and tumor-involved (red) tissues assayed by flow cytometry. **B,** Densities of major immune cell subsets compared across organ type within either tumor-free or tumor-involved tissues. **C,** Heatmap of all immune cell subsets within tumor-involved and tumor-free tissues. Transtional B cells (Trans B cell), $CD27^+IgD^+$ double-positive B cells (DP B cell), $CD27^-IgD^-$ double negative B cells (DN B cell), $CD141^+CD1c^-$ conventional type 1 dendritic cells (cDC1 DC), $CD141^-CD1c^+$ conventional type 2 dendritic cells (cDC2 DC), $CD141^+CD1c^+$ dendritic cells (DP DC), $CD141^-CD1c^-$ dendritic cells (DN DC), plasmacytoid DCs (pDC), nonclassical monocytes (NcMono), intermediate monocytes (IntMono), classical monocytes (ClassMono), $CD4^+$ regulatory T cells ($CD4^+$ Treg), $CD8^+$ resident memory T cells ($CD8^+$ TRM), $CD8^+$ effector memory RA^+ cells ($CD8^+$ EMRA), exhausted $CD8^+$ T cells ($CD8^+$ TEX), $CD8^+$ Columns are overlaid by organ type: brain (gold), liver (red), lung (blue), skin (green). Columns are also overlaid by primary tumor evaluation for being ER+, TNBC, or "mixed" (metachronous primary tumors). Tumor-free tissues are additionally annotated as adjacent (dark gold) or distant (green) to the tumor-involved tissue. Densities are depicted as *z*-scores calculated per row (each immune subset) basis with hierarchical clustering of data done by both column and row. Case numbers and tissue numbers are also depicted. Statistics generated by Wilcoxon rank sum tests (**A**) or Kruskal–Wallis test by ranks (**B**). Calculated *P* values are displayed as *, $P < 0.05$; **, $P < 0.01$; ***, $P < 0.001$; ****, $P < 0.0001$. Error bars represent the standard error of the mean (SEM). (Created with BioRender.com).

50. Eight patients were diagnosed with infiltrating ductal carcinoma and one patient with lobular carcinoma at the time of primary disease. Three patients had triple-negative breast cancer (TNBC) primary tumors, five had HR^+ primary tumors, and one had metachronous HR^-, $HER2^+$, and HR^+ primary tumors (denoted as primary tumors with "mixed" HR status in figures). Tissue procurement captured grossly tumor-involved and tumor-free tissues from five of the most common organ sites of breast cancer metastasis: bone, brain, liver, lung, and skin. Among the nine patients, eight had lung metastases, seven had liver metastases, seven had bone metastases, four had skin metastases, and four had brain metastases (**Fig. 1A**). Multifocal metastases to the same organ were sub-sampled when possible. Of the four patients with metastases to the brain, three patients had parenchymal metastases, and one patient had parenchymal and leptomeningeal metastases. Tumor-free tissues were composed of adjacent (proximal to tumor-involved tissue) and distant (contralateral or completely disease-free) tumor-free tissue sites (**Fig. 1B**). We assessed 107 pathology-validated and quality-controlled tumor tissues in total (**Fig. 1C**).

Immune densities within tumor-involved and tumor-free tissue sites

We performed flow cytometry on single-cell suspensions after tissue digestion to rapidly assess the immune TME composition of multiple collected tissues. Four flow cytometry panels were developed to interrogate the presence of $CD8^+$ T-cell, $CD4^+$ T-cell, B-cell, NK-cell, monocyte/macrophage, DC, and granulocyte subsets (subset details and gating strategies Supplementary Figs. S1 and S2). Densities of immune subsets were quantified by assessing fixed brain, liver, lung, and skin tissue volumes with measured weights. We found no differences in the densities of B cells, $CD4^+$ T cells, $CD8^+$ T cells, NKT cells, NK cells, and $CD33^+$ myeloid cells between tumor-involved metastatic tissues and matched tumor-free tissues (**Fig. 2A**). This held true for nearly all immune subsets assayed across all tissue types (Supplementary Fig. S3). Exceptions to this were increased numbers of naïve $CD4^+$ T cells in tumor-free skin, increased plasmacytoid DCs (pDC) in tumor-free brain, and increased naïve B cells in tumor-free brain as compared with their tumor-involved counterparts.

In contrast, stratifying by organ type revealed significant differences in immune densities in tumor-involved and tumor-free tissues. Lung tissues demonstrated the greatest immune cell abundance, with lung metastases having significantly more B cells, $CD4^+$ T cells, $CD8^+$ T cells, NKT cells, and NK cells than brain, liver, and skin metastases (**Fig. 2B**; Supplementary Figs. S4 and S5). Similarly, lung metastases had greater numbers of myeloid cells than brain and skin metastases, but not liver metastases. These same overall trends were observed in tumor-free tissue sites, thereby identifying the tumor metastasis organ site as a major feature dictating immune abundance. We observed low densities of immune cells in skin tissues, with B cells and NKT cells being especially scarce. Brain tissues had low numbers of immune cells, particularly B, NKT, and NK cells. The hierarchical clustering of flow cytometry data clearly delineated lung tissues as the most immune infiltrated, followed by liver tissues, brain, and skin tissues (**Fig. 2C**). No apparent association with the primary tumor HR status was observed. Abundance of immune subset infiltration was consistently elevated in lung tissues across nearly all immune subsets assayed. Exceptions to this were transitional B and plasma B cells, less commonly found in any tissue type. Moreover, we noted distant tumor-free tissues exhibited similar immune subset densities to adjacent tumor-free tissues and tumor-involved tissue sites. Consistent with these findings, paired analyses of patient-matched samples found similar levels of immune infiltrate across tumor-involved and tumor-free tissues (Supplementary Fig. S6). Although patient heterogeneity in metastatic presentation limited rigorous statistical testing, paired analyses across organ types confirmed a pattern of higher immune abundance in lung tissues and lowest immune abundance in skin tissues (Supplementary Fig. S7; Supplementary Table S4).

Immune microenvironment of metastasis is imparted by the surrounding tissue

We next sought to confirm and further explore our findings about immune abundance in different tissue sites via multiplex immunofluorescence (mIF). FFPE tissues were stained for the presence of $CD8^+$ T cells, $CD4^+$ T cells, $FOXP3^+CD4^+$ T cells, $CD68^+$ macrophages, and $CD20^+$ B cells (representative images Supplementary Figs. S8 and S9). mIF assessment of total tissue densities corroborated that immune abundance was not reduced in tumor-involved tissues as compared with tumor-free tissues across all organs (Supplementary Fig. S10A). An exception to this was slightly higher numbers of $CD20^+$ B cells in tumor-free lung tissues than in tumor-involved lung tissues.

Many of the metastatic specimens collected contained tumor-involved tissue and surrounding tumor-free regions at varying proportions (Supplementary Fig. S10B). This allowed us to assess immune infiltration into metastatic tissues in the context of both the tumor area and adjacent tumor-free tissue (**Fig. 3A**). "Clean" tumor areas within grossly positive tumor tissues were identified with guidance from pathologist assessment of paired H&E images (**Fig. 3B** and **C**). Within clean tumor areas, tumor cancer islands and surrounding stroma were further segmented. To examine the relationship between tumor tissues and adjacent tumor-free tissue, we created serial bands of tumor-adjacent areas with 100 μm diameters extending to 500 μm from the borders of the clean tumor area. The tissue area beyond 500 μm of the clean tumor was termed "adjacent tumor-free" tissue. This approach yielded eight spatially distinct regions: cancer islands, intratumoral stroma, proximal 0 to 100 μm, proximal 100 to 200 μm, proximal 200 to 300 μm, proximal 300 to 400 μm, proximal 400 to 500 μm, and adjacent tumor-free.

We observed significant variability in the relative proportion of tumor stroma composed within clean tumor areas across all organ sites (Supplementary Fig. S10C). In fact, we found nearly no quantifiable stromal areas within some metastatic tissues within clean tumor areas, perhaps reflecting the aggressive and proliferative nature of metastatic cancer cells. Given the lack of quantifiable intratumoral stromal area in several tissue sites, we next compared the relative areas of intratumoral stroma and tumor proximal stroma, as defined as either a surrounding 100 μm band (Supplementary Fig. S10D) or 200 μm band (Supplementary Fig. S10E). Intratumoral stroma tended to make up the majority of tumor stroma in bone and skin organs in which proximal stroma was identified. Intratumoral stroma also made up the majority of tumor stroma in liver tissues, although 100 and 200 μm proximal stroma still made up an average of 25% and 35% of tumor stroma, respectively. Proximal stroma comprised the largest fractions of tumor stroma in brain and lung tissues, with 100 and 200 μm proximal stroma often making up more than 50% of tumor stroma. Together, this data demonstrated that the proximal stroma is a major interaction site between cancer cells and immune cells in metastatic tumor microenvironments.

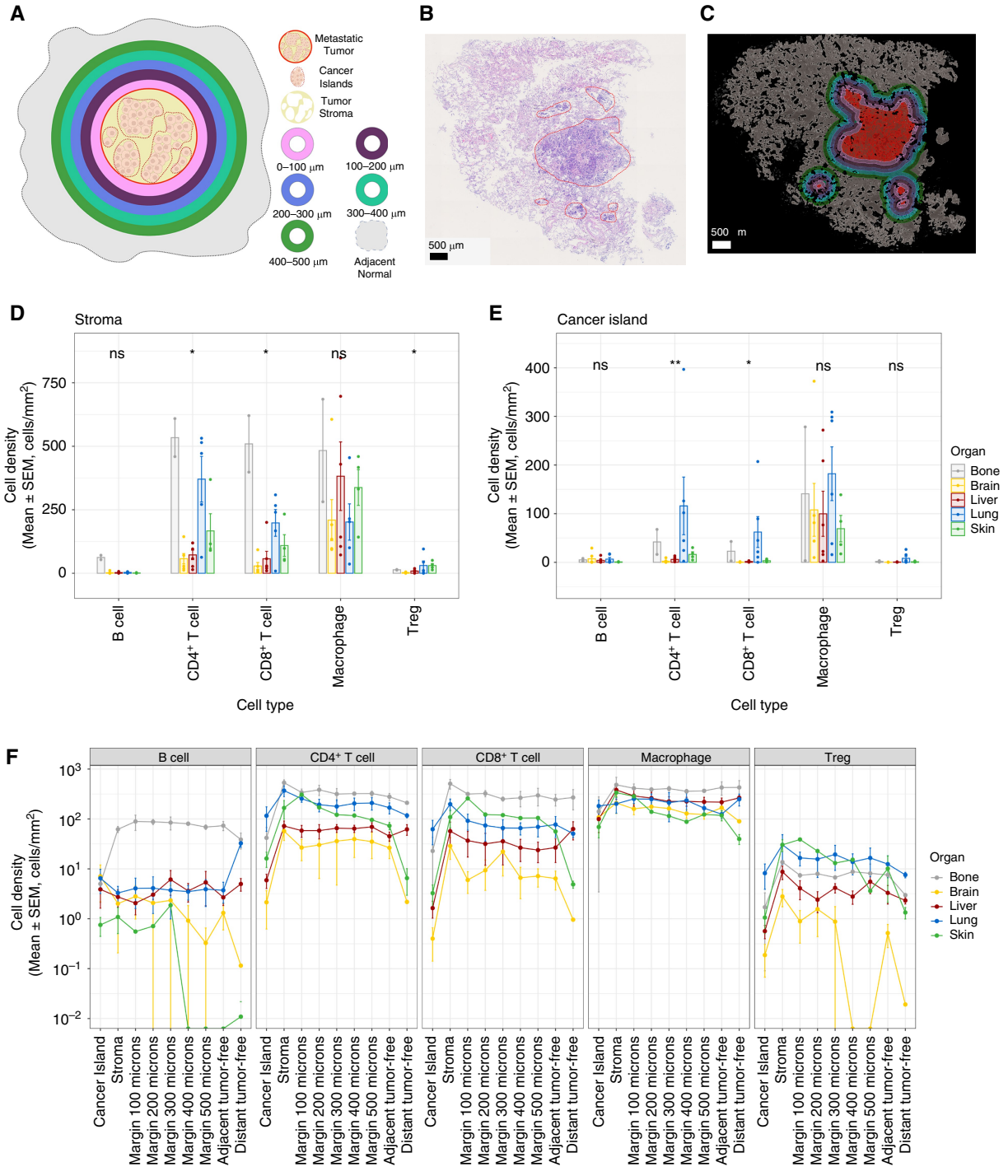

Figure 3.

Immune densities within metastatic tumor stroma reflect surrounding immune density of surrounding tissue. **A,** Cartoon schematic of tissue segmentation approach for whole slide multiplex immunofluorescence (mIF) imaging of tumor-involved tissues. Metastatic tumor-involved areas of tissues were manually identified, within which cancer island and tumor stroma were identified. Tumor proximal areas of 100 μm increments were generated up to 500 μm. Tissue beyond 500 μm was defined as surrounding tumor-free tissue. **B,** Representative image of pathologist-guided selection of clean tumor areas circled in red. **C,** Representative image of tissue segmented areas of tumor-involved lung tissue. Cell densities of B cells ($CD20^+$), $CD4^+$ T cells, $CD8^+$ T cells, macrophages ($CD68^+$), and regulatory T cells (CD4+ $FOXP3^+$) T cells were quantified in the **D**, stroma and **E**, cancer islands of tumor-involved tissues. The mean and the standard error of means are shown. **F,** Cell densities of immune subsets within segmented regions of metastatic tumors, adjacent tumor-free tissue, and distant tumor-free tissue are shown for each organ type. Statistics generated by Kruskal–Wallis test by ranks (**F**). Calculated *P* values are displayed as *, $P < 0.05$; **, $P < 0.01$. Error bars represent SEM. (Created with BioRender.com).

Next, we examined immune densities within our established spatially segmented TME regions. In general, the organ site of metastasis dictated the abundance of the tumor infiltrate with bone and lung metastases having the highest densities of $CD4^+$ and $CD8^+$ T cells in tumor stroma (**Fig. 3D**; Supplementary Figs. S10F and S11). The tumor stroma of bone metastases had the highest average abundances of $CD20^+$ B cells, $CD4^+$ T cells, $CD8^+$ T cells, and macrophages. The tumor stroma of the brain had numerous macrophages but low numbers of B cells, $CD4^+$ T cells, and $CD8^+$ T cells. Tumor stroma in skin metastases had higher numbers of $CD8^+$ T cells than in brain metastases and higher numbers of $FOXP3^+CD4^+$ T cells than in brain and liver metastases. Lung metastases demonstrated the most significant differences in immune abundance, with higher densities of $CD4^+$ T cells in tumor stroma compared with brain and liver metastases. Furthermore, cancer island localized $CD4^+$ and $CD8^+$ T cells were most abundant in lung metastases (**Fig. 3E**). Extending beyond the segmented tumor area, we observed consistent immune subset densities from the intratumoral stroma into adjacent tumor-free tissue and distant tumor-free tissue (**Fig. 3F**). Together this data stresses the importance of adjacent tumor-free tissue in establishing immune densities of metastatic tumors.

Lung tissues have increased densities of conventional type 1 DCs

Given the propensity of tumor-involved and tumor-free lung tissues to have significantly greater immune cell infiltrates than liver tissues, we next asked what immune cell subsets might be key to this. Therefore, we compared immune densities between tumor-free lungs and tumor-free livers to examine premetastatic immune infiltration tendencies. Of all immune subsets compared, conventional type 1 $CD141^+$ $CD1c^-$ DCs (cDC1) were the immune cell subtype most significantly enriched in tumor-free lung tissues as compared with tumor-free liver tissues (**Fig. 4A**). This was followed by $CTLA\text{-}4^+$ regulatory T cells (Treg), $PD\text{-}L1^+$ cDC1 DCs, $TIGIT^+$ Tregs, pDCs, $CD8^+$ tissue-resident memory T cells (TRM), $CD11c^+$ $CD141^-$ $CD1c^-$ double negative (DN) DCs, and $CD141^+CD1c^+$ double-positive (DP) DCs; all indicative of lung tissues being a site of active and ongoing immune responses. These variables also significantly differed between tumor-involved lung and liver tissues.

Lung tissues demonstrated higher densities of all 4 identified phenotypes of cDCs (**Fig. 4B**; Supplementary Fig. S12A) compared with other metastatic tissue sites, except for higher densities of conventional type 2 $CD141^-$ $CD1c^+$ DCs (cDC2) and DP DCs in brain tissues. Given that lung tissues have higher infiltrates of nearly all immune subsets, we next compared frequencies of cDC subtypes (**Fig. 4C**; Supplementary Fig. S12B). Tumor-free and tumor-involved lung tissues had higher frequencies of cDC1s than liver, brain, and bone metastases but similar frequencies as skin tissues. To further examine the functional status of tissue DCs, we assessed PD-L1 expression as a marker of increased DC activation and antigen presentation (16). Compared with other metastatic sites, tumor-involved lungs had significantly higher frequencies of PD-L1–expressing cells of all cDC subsets (**Fig. 4D**; Supplementary Fig. S12C). In tumor-free tissues, cDC1s in the lungs had significantly higher frequencies of PD-L1–expressing cells than those in the liver, bone, and brain. We also observed that tumor-involved lung monocyte/macrophage subsets expressed more PD-L1 than those in other tissue sites, suggesting that the lung TME may be uniquely predisposed to foster myeloid antigen-presenting cell activation and maturation (**Fig. 4E**; Supplementary Fig. S12D).

Immune composition in the context of tumor pathological characteristics

We next explored how immune composition might be defined by organ type and how this immune composition is associated with pathological features of the metastatic tumor. To do so we performed unsupervised clustering of tissue samples with the densities of 34 complex immune subsets being used as input variables (Supplementary Fig. S13A–S13C). We identified five major "clusters" of tissues, with cluster 1 mostly being composed of liver tissues, cluster 2 mostly being composed of lung tissues and some liver tissues, cluster 3 entirely being composed of lung tissues, cluster 4 entirely being composed of tumor-free brain tissues, and cluster 5 being composed of brain, skin, and liver tissues (Supplementary Fig. S13D). Generally, tissue sites are segregated by graded degrees of immune infiltration (Supplementary Fig. S13E). Cluster 2 and cluster 3 were identified as "warm" and "hot" tissue types, respectively, with high densities of all immune subsets. Cluster 1 and Cluster 5 reflected "cold" and "coldest" tissues. Cluster 4, composed of tumor-free brain tissues, was defined by monocyte/macrophages, dendritic cells, and some $CD8^+$ T cells. Each cluster was composed of tissues from several patient cases, highlighting both significant interpatient and intrapatient heterogeneity in the immune composition of metastatic sites (Supplementary Fig. S13F and S13G). However, tumor-involved tissues within these clusters demonstrated some trends in the expression of ER, PR, HER2, and Ki-67 (Supplementary Fig. S13G–S13J). Tumors in cold cluster 1 tended to be ER^+, PR^-, $HER2^{low}$, and tumors in coldest cluster 5 tended to be ER^-, PR^-, $HER2^-$. Tumors in hot cluster 3 tended to be ER^+, PR^+, and $HER2^-$ with high percentages of $Ki\text{-}67^+$ cells (Supplementary Fig. S13K). Tumors in warm cluster 2 tended to be ER^+, PR^-, and $HER2^-$. Thus, these data demonstrate that abundant immune infiltrate can be observed in ER^+PR^+ metastases, and the degree of immune infiltrate may positively correlate with Ki-67 expression.

Distinct immune composition across metastatic tissue sites

With a firm understanding that immune densities were dictated by organ type, we next asked how immune subset composition varied across the TME of different metastatic sites. We observed several differences in subset frequencies of the major immune subsets across organ types (Supplementary Figs. S14 and S15). Naïve T cells were highest in bone tissues. Lung tissues had higher frequencies of $CD45RA^+$ effector memory (EMRA) $CD8^+$ cells, whereas liver tissues had higher frequencies of $CD69^+CD8^+$ "pre"-tissue-resident memory cells. Memory B cells and plasmablasts were highest in lung tissues, with naïve B cells being frequent in liver, lung, and bone tissues. Mature NK cells tended to be diminished in liver tissues, and terminal NK cells were more frequent in brain tissues. Classical monocyte frequency was highest in bone and liver tissues, with intermediate monocyte/macrophages being most frequent in brain tissues.

To gain a broader perspective of overall immune composition, we examined the frequency of tumor-infiltrating immune cell subsets among total immune cells (**Fig. 5A**). Bone metastases were predominantly composed of neutrophils and other granulocytes. Brain metastases were dominated by monocyte/macrophages, followed by $CD8^+$ T cells and NKT cells. Liver, lung, and skin metastases were heavily infiltrated by neutrophils, and skin metastases also demonstrated infiltration by other granulocytes. Frequencies of other immune subsets varied across tissue sites, with $CD4^+$ T cells and NK cells being the most frequent in lung metastases and $CD8^+$ T cells being the most frequent in lung and skin metastases.

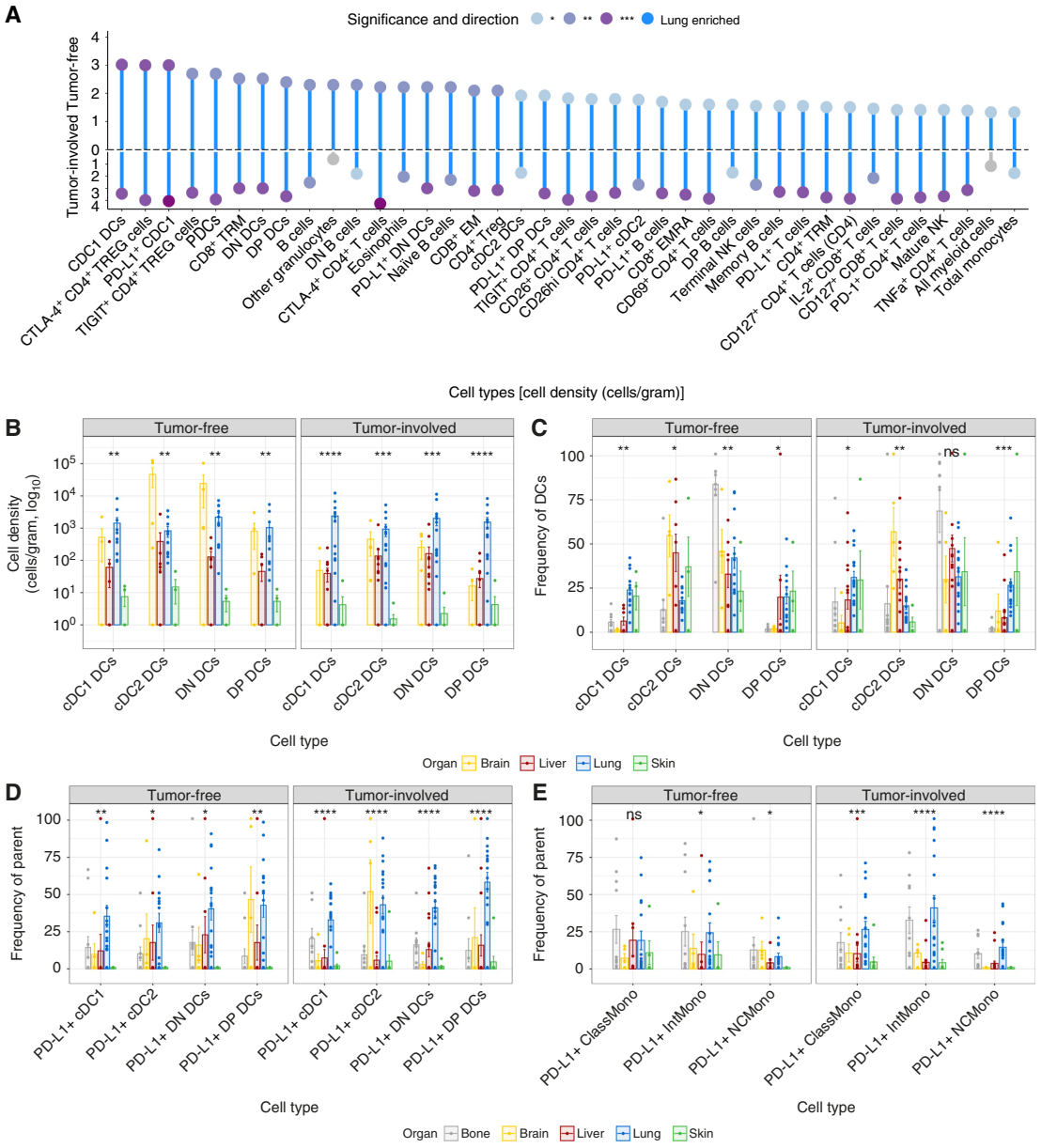

Figure 4.

Conventional type 1 dendritic-cell densities are a key feature of tissue immune density setpoints. **A,** Matchstick plot depicts *P* values of significant differences between lung and liver tissues in densities for all immune subsets and complex immune subsets identified. Analysis includes CTLA-4, PD-1, PD-L1, TIGIT, and TNF-α expression on relevant cell types. Negative $\log_{10}$ transformed *P* values are displayed and sorted from most significant to least significant within the tumor-free tissues. Blue lines indicate a greater density in lung tissue as compared with liver tissues. **B,** Densities of dendritic-cell (DC) subsets, and **C**, frequency of DC subsets among total conventional DCs were compared across organ type within either tumor-free or tumor-involved tissues. Statistics generated by Wilcoxon rank sum tests (**A**) or Kruskal–Wallis test by ranks (**B–E**). Calculated *P* values are displayed as *, $P < 0.05$; **, $P < 0.01$; ***, $P < 0.001$; ****, $P < 0.0001$. Error bars represent SEM. (Created with BioRender.com).

Neutrophils were the most common immune cell subset in bone, liver, lung, and skin metastases. Liver metastases specifically had the highest frequency of neutrophils within tumor-infiltrating immune cells (**Fig. 5B**). In contrast, brain metastases had rare but detectable numbers of neutrophils. To rule out that neutrophils were simply within the vasculature of metastases, we validated the presence of tumor-infiltrating neutrophils by staining tissues for $CD66b^+$ cells. Robust neutrophil infiltration was observed within tumor areas and among other immune subsets, such as $CD3^+$ T cells in multiple tissue types (**Fig. 5C**). Furthermore, $CD66b^+$ cells often had observable polymorphonuclear morphology with "horseshoe" nuclear shapes, confirming their identity as neutrophils.

Immune cell source of PD-L1 expression varies by tissue site

Discordant expression of PD-L1 has been reported between primary tumors and metastases and between different metastatic

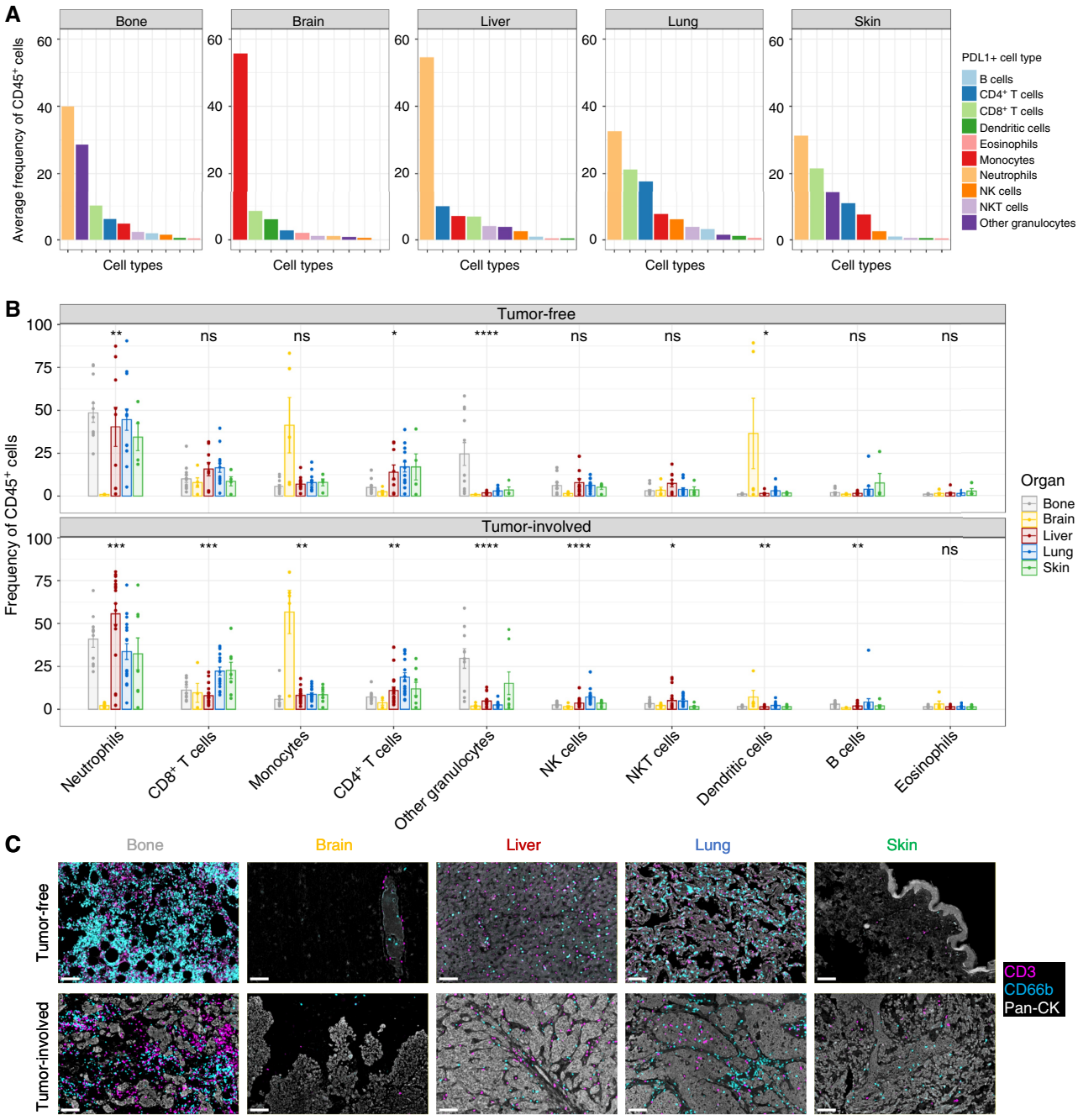

Figure 5.

Neutrophils are a predominant immune cell subset in bone, liver, lung, and skin metastases. **A,** Bar plots of the average density of all major immune subsets (B cells, CD4$^+$ T cells, CD8$^+$ T cells, DCs, eosinophils, neutrophils, NKT cells, other granulocytes, monocyte/macrophages, and NK cells) for tumor-involved bone, brain, liver, lung, and skin tissues. **B,** Frequencies of all major immune subsets among total CD45$^+$ immune cells in tumor-free and tumor-involved tissues compared across organ types. **C,** mIF images of tumor-free and tumor-involved tissues stained for neutrophils (CD66b$^+$) in the context of CD3$^+$ T cells and cancer cells (pan-cytokeratin$^+$; pan-CK$^+$). Scale bars shown represent 100 μm. Statistics generated by Kruskal–Wallis test by ranks (**B**). Calculated *P* values are displayed as *, $P < 0.05$; **, $P < 0.01$; ***, $P < 0.001$; ****, $P < 0.0001$. Error bars represent SEM. (Created with BioRender.com).

sites (17, 18). In line with these previous studies, we found PD-L1 expression (as a percentage of immune stroma) to be higher in lung and liver metastases as compared with those in bone marrow, brain, and skin (Supplementary Fig. S16A and S16B). To determine if PD-L1 expression levels might correlate with increased immune infiltrate, we next sub-grouped metastatic samples into

PD-L1$^+$ (≥1%) and PD-L1$^-$ (<1%) and examined our collected immune data in this context. We found no differences in densities of lymphocyte subsets in brain, lung, or skin metastases (Supplementary Fig. S16C). Moreover, we found higher T-cell, NKT-cell, and NK-cell infiltration in PD-L1$^-$ liver metastases than PD-L1$^+$ liver metastases. We then examined T-cell functional status in PD-L1 tissue expression, given that increased TME PD-L1 has been linked to T-cell exhaustion. Across all tissue sites, we found no differences in the capacity of CD8$^+$ T cells or CD4$^+$ T cells to secrete IFNγ, TNFα, or IL2 (Supplementary Fig. S16D and S16E).

Given the degree of heterogeneity we found in immune cell composition between different tissue sites, we next asked how this might affect the context of PD-L1 expression. We found that PD-L1 expression was identifiable on various immune cell subsets in tumor-free and tumor-involved tissues (**Fig. 6A**). PD-L1 was most predominantly expressed by neutrophils, followed by other myeloid cells such as classical monocytes and intermediate monocytes/macrophages (**Fig. 6B**). PD-L1 expression on a variety of myeloid cells was also observed in multiple tumor-free tissues (Supplementary Fig. S16F). In liver metastases, 50% of PD-L1 expression on identified immune cells was expressed by tumor-infiltrating neutrophils (Supplementary Fig. S16G). Conversely, in brain metastases in which neutrophils are far less abundant, PD-L1 was predominantly expressed by intermediate monocytes/macrophages and cDC2s. mIF staining of liver and lung tissues confirmed PD-L1 expression on tumor-infiltrating neutrophils in lung and liver metastases (**Fig. 6C**).

Influence of tumor infiltration on immune cell composition

We next examined how tumor infiltration perturbs immune composition by comparing immune subset frequencies between tumor-free and tumor-involved tissues of the same organ type. In bone metastases, we observed an increase in HLA-DR^{low} cells within nonclassical monocytes (NcMono) and an increase in DCs among all immune cells (Supplementary Figs. S17A and S17G). In brain metastases, we observed an increase of intermediate monocytes among monocyte subsets (Supplementary Fig. S17B and S17F). We found increased CD8$^+$ T cells in skin metastases among CD3$^+$ T cells (Supplementary Fig. S17C). In liver metastases, we observed an increase in Tregs, CD16$^-$ granulocytes, TIGIT$^+$ Tregs, CTLA-4$^+$ Tregs, naïve CD4$^+$ T cells, CD8$^+$ TRM, HLA-DR^{low} NcMono, and naïve B cells (**Fig. 7A**; Supplementary Fig. S17D, S17E, and S17G–S17I). In lung metastases, we observed an increase in intermediate monocytes, CD8$^+$ effector memory (EM), and CD8$^+$ EMRA (**Fig. 7B**; Supplementary Figs. S17D and S17F). Thus, not only do immune densities differ across organs, but so do certain organ-

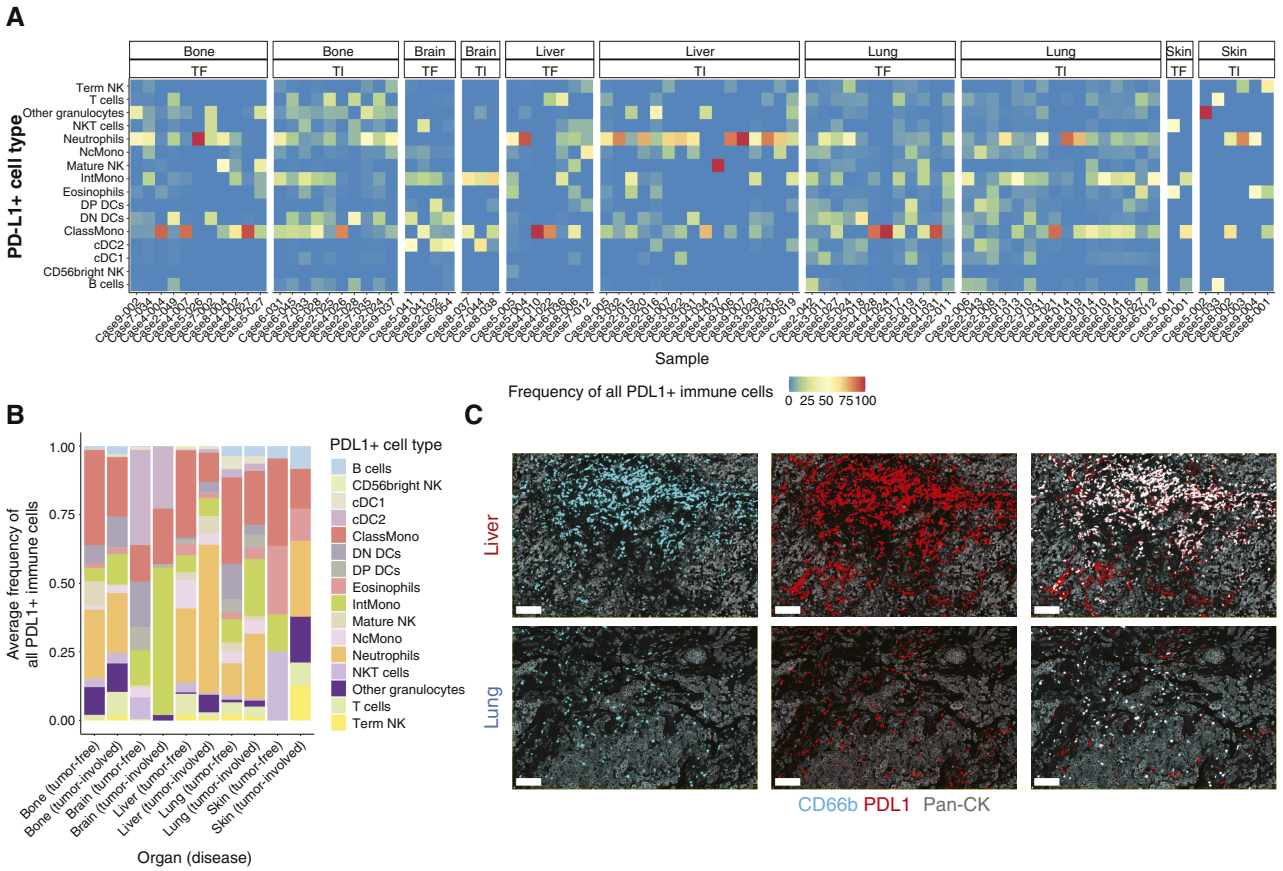

Figure 6.

Neutrophils are a substantial source of PD-L1$^+$ cells in metastatic tumors. **A,** Heatmap depicting the frequency of all PD-L1$^+$ immune cells made up of the relevant immune cell subsets. **B,** Average frequency of each immune cell subset within PD-L1$^+$ immune cells is displayed for tumor-free and tumor-involved tissues. **C,** Representative mIF images of CD66b (cyan) and PD-L1 (red) staining in tumor-involved liver and lung tissues. The scale bars shown represent 100 μm. (Created with BioRender.com).

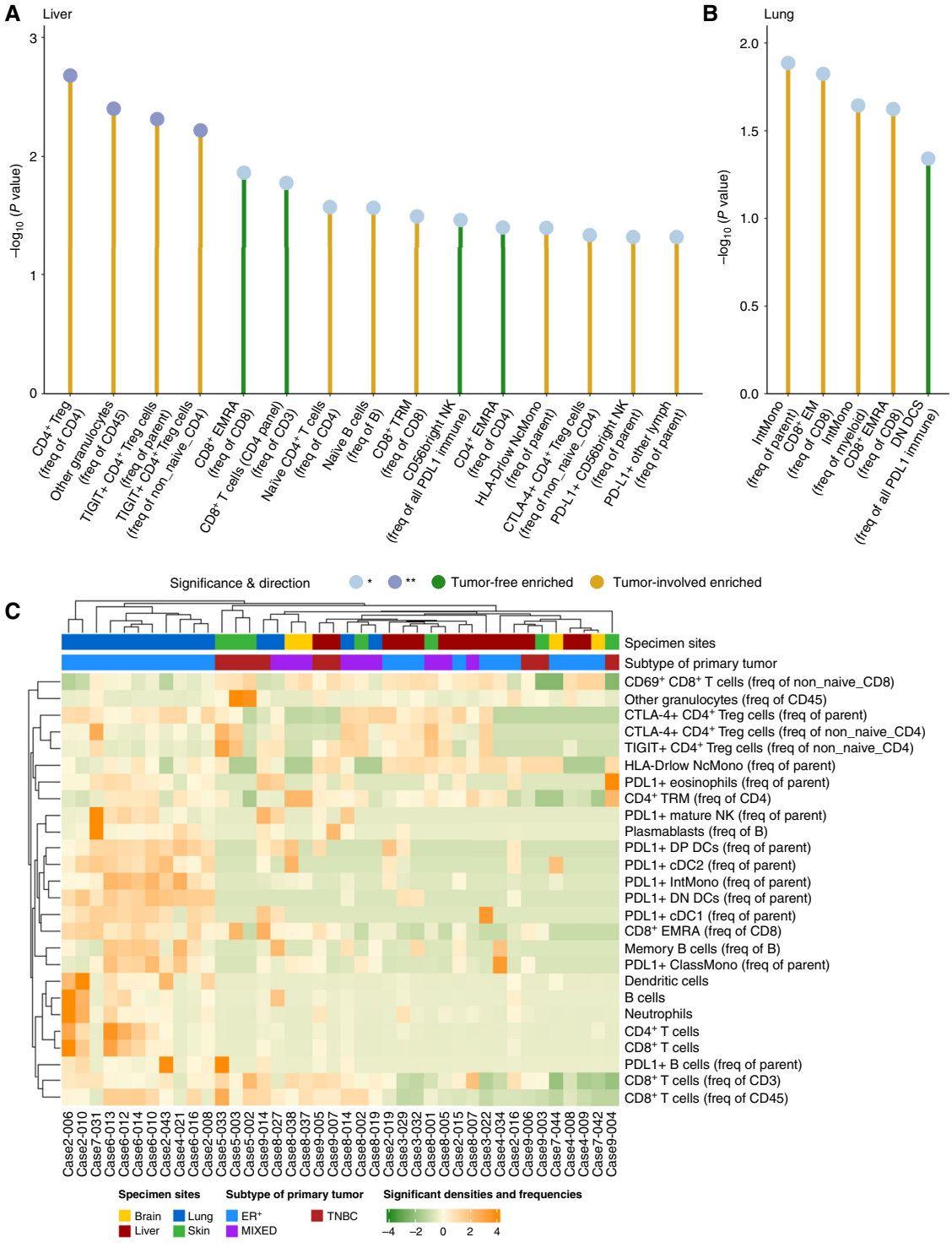

Figure 7.

Altered phenotype of tissue immune infiltrate in metastatic tissues. Matchstick plots depict *P* values of significant differences between tumor-free and tumor-involved (**A**) liver and (**B**) lung tissues for all immune subset densities and frequencies assessed. Negative $\log_{10}$ transformed *P* values are displayed and sorted from most significant to least significant within the tumor-free tissues. Yellow lines indicate a greater density/frequency in tumor-involved tissue as compared with tumor-free tissues, whereas green lines indicate a greater density/frequency in tumor-free tissue as compared with tumor-involved tissues. **C,** Hierarchical clustering plot of tumor-involved tissues based on all significant immune variables that were identified by comparing tumor status and organ type. Specimen organ types are overlaid. Statistics generated by Wilcoxon rank sum tests (**A** and **B**). (Created with BioRender.com).

specific immune microenvironment responses to metastatic tumor infiltration.

Given that T-cell dysfunction is a key feature of immune escape, we additionally interrogated the differentiation, effector, and functional phenotypes of metastatic tumor-infiltrating T cells. Neither $CD4^+$ nor $CD8^+$ T-cell subsets showed any variation between organ type matched tumor-free and tumor-involved tissues in their expression of differentiation markers CD127 and KLRG-1, the activation marker CD69, checkpoint molecules CTLA-4, PD-1, and TIGIT (Supplementary Figs. S18A and S18B). Additionally, we observed no decreased functional capacity of $CD4^+$ or $CD8^+$ T cells to produce cytokines IL2, IFNγ, or TNFα (Supplementary Figs. S18C and S18D). This data was corroborated by the low frequencies of detectable $PD\text{-}1^+CD39^+$ exhausted $CD8^+$ T cells in most tissue sites (Supplementary Fig. S17D). Therefore, we observed minimal signs of ongoing tumor-induced T-cell exhaustion or dysfunction in metastatic tissues.

Finally, we sought to generate a comprehensive visualization of all the key features that define the organ-specific features of the metastatic TME. Our data show two axes drive these features: (i) how immune composition differs across organ sites and (ii) how immune composition differs between tumor-involved and tumor-free tissues. Thus, to construct a visual of all key metastatic TME variables, we generated a heatmap that was composed of data significantly different when compared in this way (**Fig. 7C**). Lung metastases demonstrated an abundance of multiple tumor-infiltrating immune subsets, along with increased frequencies of memory B cells, plasmablasts, and PD-L1–expressing antigen-presenting cells. In contrast, liver metastases demonstrated lower numbers of tumor-infiltrating immune cells, higher fractions of activated Tregs, and increased fractions of $HLA\text{-}DR^{low}$ monocytes. Our data identify lung tissues as uniquely distinct from the brain, bone, liver, and skin in their capacity to generate immune recruitment and activation.

Discussion

MBC is heterogeneous between and within patients at genetic, molecular, and clinical levels (19). Given that most patients with MBC are currently not indicated for treatment with ICIs because of lack of PD-L1 expression, an improved understanding of antitumor immunity in MBC is greatly needed (20). Unraveling immune infiltration patterns in MBC tissues has proved challenging and represents a major barrier to successful immunotherapy design and treatment. Although TNBC tumors have been shown to have greater immune infiltration than HR^+ breast cancer tumors, these data are largely derived from primary tumors (21). A major finding of our study is that the organ site of metastases is another critical variable in dictating the immune composition of breast cancer metastases. In parallel, recent studies across various cancer types demonstrated organ-specific differences in clinical response to immunotherapy (22–28). Furthermore, we show that metastases' immune compositions mirror adjacent nontumor tissues. These findings have important implications for evaluating patient tumor biopsies and designing immunotherapy strategies that may need to be tailored based on the organ location of metastasis. Evidence from our study and several others now clearly points to the necessity for studying the "Immunostat" of metastasis in an organ-specific context (29, 30).

Our findings that immune cell phenotypes and quantity largely reflect that of adjacent disease-free tissue are somewhat surprising. However, although our study focuses on metastatic tissues across several tissue sites, most immune TME profiling studies have focused on primary tumor samples (31–33). A limitation of our study is that our samples are restricted to patients with lethal breast cancer and may not reflect immune dynamics in all patients with MBC. Our findings possibly reflect that of "immune escaped" MBC at the terminal end of the metastatic disease continuum. In contrast, early-stage tumors have increased immune infiltrate relative to adjacent normal tissues (34). Although MBC metastases generally exhibit decreased immune infiltration as primary tumors (7, 35, 36), the extent to which these findings are because of heavy pretreatment, immunoediting, or other factors is unclear (37, 38). Tumor remodeling and evolution under the pressures of therapy and immune editing severely complicates our understanding of tumor immune composition in MBC (39, 40). Future studies that uncover the coevolution of cancer and immune cell subsets through the entire continuum of disease progression will be an invaluable next step for the field.

Organ-specific infiltration patterns of immune cell subsets have also recently been reported in studies of lung cancer, colorectal cancer, and melanoma metastases (41–43). Moreover, organ-specific features of immune cell subsets such as NK cells, tissue-resident macrophages, and tissue-resident T cells have been observed (44–47). Innate immune cells, in particular, have long been noted to have organ-specific features dictated by inter-organ differences in nutrients, tissue homeostasis, and embryonic origins (48). We show lung tissues have more abundant immune infiltration than liver, brain, and skin tissues. We find that the presence of cDC1s is central to this phenomenon. Compared with lung tissues, skin tissues had less abundant cDC1s, and brain and liver tissues had increased fractions of cDC2s relative to cDC1s. cDC1s, marked by the transcription factor Batf3, are a critical determinant of T-cell recruitment and priming in tumor tissues (49–51). Enrichment of cDC1s in the lung may increase immunosurveillance of tumor metastasis (52). Thus, our findings suggest that a preexisting lack of cDC1s represents a substantial hurdle for immunotherapy of nonlung metastatic tumors.

Bone and liver metastases also demonstrate distinct immunosuppressive features. Both bone and liver metastases show increased fractions of $HLA\text{-}DR^{low}$ cells among $CD16^+CD14^{low}$ nonclassical monocytes/macrophages. In line with this, elevated systemic levels of $HLA\text{-}DR^{low}CD16^{+/-}CD14^+$ monocytes, often described as the monocytic subset of myeloid-derived suppressor cells, have been correlated with liver and bone metastasis in patients with MBC (53, 54). We also observed increased frequencies of activated Tregs, marked by expression of TIGIT and CTLA-4, in liver metastases. In parallel, recent preclinical studies pointed to the role of liver metastasis localized Tregs and myeloid cells in inhibiting systemic antitumor immunity (55, 56). Future studies are needed to clarify how the interplay between T cells, Tregs, and myeloid cells in the TME may drive reduced survival often observed in patients with MBC with liver metastases (57).

Another major finding of this study is that neutrophils are abundant in MBC tumors, especially liver and lung tumors. Moreover, they are a significant source of PD-L1 expression in these tissues. Evidence for roles in both pro- and antitumor immunity exists for neutrophils (58, 59). Various findings have shown the capacity of the TME features to polarize neutrophils in ways that may either promote or resist metastatic progression (60). In patients with MBC, a higher neutrophil-to-lymphocyte ratio in peripheral blood is a negative

prognostic factor (61). Conversely, recent studies have highlighted neutrophil's critical role in cancer cell cytotoxicity in patients treated with immunotherapy (62, 63). Further studies are warranted to evaluate the role of tumor-infiltrating neutrophils in MBC, especially in the context of tissue site and immunotherapy response.

Understanding mechanisms of therapeutic resistance in metastatic TME has been stymied by challenges relating to a lack of adequate tissues to interrogate their complexities properly. Metastatic tissue biopsies for research studies are infrequently performed, often lack sufficient cellularity, and may be biased to certain tissue sites by ease of access (i.e., axillary masses and skin metastases). Additionally, single-tissue biopsies fail to encompass the heterogeneity and scope of multifocal metastatic disease. Our study's rapid tissue procurement of difficult-to-access tissue sites enabled important hypotheses to generate immune characterization of the metastatic TME. Our findings are limited by the small number of patients assessed and the limited number of specimens from brain, skin, and bone metastases. It is also unclear how artifacts and circumstances of patient death affect the experimental assessment of TME immune composition. Nevertheless, rapid postmortem tissue procurement programs provide a valuable means of advancing immune-oncology research, and studies have shown a relatively minimal impact of death on the biological profiles of collected tissues (64–69). Further studies in larger cohorts of metastatic tumor tissues are needed to validate and expand upon our findings.

A complex challenge is how patient treatment algorithms should personalize therapeutic regimens based on genomic, immune, and location of metastatic spread. Understanding how immunosurveillance evolves throughout treatment will be critical in developing immunotherapies that improve progression-free survival. Our study demonstrates that organ-specific features of immune composition should be a key consideration when evaluating metastatic tissue biomarkers, and stratification by organ site should be reported in clinical trial response data. Heterogeneous therapeutic responses within and between patients continue to be a major challenge in treating multifocal metastatic disease. In the rapidly advancing era of precision medicine, our findings highlight the importance of clinical care that utilizes immunotherapeutic strategies based on metastases' location and immune composition. However, given the infeasibility of collecting multiple tissue biopsies simultaneously, new and noninvasive methods, such as ImmunoPET or cfDNA, will become increasingly important shortly when making these precision-based clinical decisions (70). Moreover, future studies are urgently needed to identify mechanisms of organ-specific resistance to immunotherapy and to design therapeutic strategies with improved pathological responses across multifocal metastatic disease.

Authors' Disclosures

No disclosures were reported.

Authors' Contributions

C.A. Egelston: Conceptualization, data curation, formal analysis, investigation, visualization, methodology, writing–original draft, writing–review, and editing. **W. Guo:** Conceptualization, resources, data curation, formal analysis, investigation, visualization, methodology, writing–original draft, writing–review and editing. **D.L. Simons:** Investigation. **J. Ye:** Investigation. **C. Avalos:** formal analysis, investigation. **S.T. Solomon:** Investigation. **M. Nwangwu:** resources, software, formal analysis. **M.S. Nelson:** Resources, software, formal analysis. **J. Tan:** Investigation. **E.R. Bacon:** Conceptualization, resources, funding acquisition, investigation. **K. Ihle:** Resources, validation, investigation. **D. Schmolze:** Investigation. **L. Tumyan:** Investigation. **J.R. Waisman:** Conceptualization, resources, supervision, funding acquisition. **P.P. Lee:** Conceptualization, resources, supervision, funding acquisition, writing–original draft, writing–review and editing.

Acknowledgments

The authors thank the generous donors of the Waisman Innovation Fund, which funded this work. We thank Dr. Kim Margolin for the discussion and feedback on the study findings. We thank the City of Hope Research Pathology and Analytical Cytometry cores for their support. Lastly, we offer our most sincere and enduring gratitude to our patient donors and their families who decided to give back to science and help restore health to others in need in a moment of crisis. This work was supported by the Waisman Innovation Fund. Research reported in this publication included work performed in the Analytical Cytometry Core and the Pathology Research Services Core, all supported by the National Cancer Institute of the National Institutes of Health under award number P30CA033572. The City of Hope Center for Precision Medicine also supported part of this work. The content is solely the authors' responsibility and does not necessarily represent the official views of the National Institutes of Health.

Note

Supplementary data for this article are available at Cancer Immunology Research Online (http://cancerimmunolres.aacrjournals.org/).

Received August 30, 2023; revised March 6, 2024; accepted July 23, 2024; published first July 24, 2024.

References

1. Redig AJ, McAllister SS. Breast cancer as a systemic disease: a view of metastasis. J Intern Med 2013;274:113–26.
2. Miglietta F, Bottosso M, Griguolo G, Dieci MV, Guarneri V. Major advancements in metastatic breast cancer treatment: when expanding options means prolonging survival. ESMO Open 2022;7:100409.
3. Cortes J, Cescon DW, Rugo HS, Nowecki Z, Im S-A, Yusof MM, et al. Pembrolizumab plus chemotherapy versus placebo plus chemotherapy for previously untreated locally recurrent inoperable or metastatic triple-negative breast cancer (KEYNOTE-355): a randomised, placebo-controlled, double-blind, phase 3 clinical trial. Lancet 2020;396:1817–28.
4. Schmid P, Adams S, Rugo HS, Schneeweiss A, Barrios CH, Iwata H, et al. Atezolizumab and nab-paclitaxel in advanced triple-negative breast cancer. N Engl J Med 2018;379:2108–21.
5. Emens LA, Adams S, Barrios CH, Diéras V, Iwata H, Loi S, et al. First-line atezolizumab plus nab-paclitaxel for unresectable, locally advanced, or metastatic triple-negative breast cancer: IMpassion130 final overall survival analysis. Ann Oncol 2021;32:983–93.
6. Kennecke H, Yerushalmi R, Woods R, Cheang MCU, Voduc D, Speers CH, et al. Metastatic behavior of breast cancer subtypes. J Clin Oncol 2010;28:3271–7.
7. He T-F, Yost SE, Frankel PH, Dagis A, Cao Y, Wang R, et al. Multi-panel immunofluorescence analysis of tumor infiltrating lymphocytes in triple negative breast cancer: evolution of tumor immune profiles and patient prognosis. PLoS One 2020;15:e0229955.
8. Garcia-Recio S, Hinoue T, Wheeler GL, Kelly BJ, Garrido-Castro AC, Pascual T, et al. Multiomics in primary and metastatic breast tumors from the AURORA US network finds microenvironment and epigenetic drivers of metastasis. Nat Cancer 2023;4:128–47.
9. Ogiya R, Niikura N, Kumaki N, Bianchini G, Kitano S, Iwamoto T, et al. Comparison of tumor-infiltrating lymphocytes between primary and metastatic tumors in breast cancer patients. Cancer Sci 2016;107:1730–5.
10. Zhu L, Narloch JL, Onkar S, Joy M, Broadwater G, Luedke C, et al. Metastatic breast cancers have reduced immune cell recruitment but harbor increased macrophages relative to their matched primary tumors. J Immunother Cancer 2019;7:265.

11. Hegde PS, Chen DS. Top 10 challenges in cancer immunotherapy. Immunity 2020;52:17–35.
12. Bacon ER, Ihle K, Lee PP, Waisman JR. Building a rapid autopsy program—a step-by-step logistics guide. Transl Med Commun 2020;5:23.
13. Bankhead P, Loughrey MB, Fernández JA, Dombrowski Y, McArt DG, Dunne PD, et al. QuPath: open source software for digital pathology image analysis. Sci Rep 2017;7:16878.
14. Kaufman L, Rousseeuw PJ. Partitioning around medoids (program PAM). In: Finding groups in data. New York: John Wiley & Sons, Ltd; 1990. pp. 68–125.
15. Bacon ER, Ihle K, Guo W, Egelston CA, Simons DL, Wei C, et al. Tumor heterogeneity and clinically invisible micrometastases in metastatic breast cancer—a call for enhanced surveillance strategies. NPJ Precis Oncol 2024;8:81.
16. Peng Q, Qiu X, Zhang Z, Zhang S, Zhang Y, Liang Y, et al. PD-L1 on dendritic cells attenuates T cell activation and regulates response to immune checkpoint blockade. Nat Commun 2020;11:4835.
17. Boman C, Zerdes I, Mårtensson K, Bergh J, Foukakis T, Valachis A, et al. Discordance of PD-L1 status between primary and metastatic breast cancer: a systematic review and meta-analysis. Cancer Treat Rev 2021;99:102257.
18. Rozenblit M, Huang R, Danziger N, Hegde P, Alexander B, Ramkissoon S, et al. Comparison of PD-L1 protein expression between primary tumors and metastatic lesions in triple negative breast cancers. J Immunother Cancer 2020; 8:e001558.
19. Pasha N, Turner NC. Understanding and overcoming tumor heterogeneity in metastatic breast cancer treatment. Nat Cancer 2021;2:680–92.
20. Gatalica Z, Snyder C, Maney T, Ghazalpour A, Holterman DA, Xiao N, et al. Programmed cell death 1 (PD-1) and its ligand (PD-L1) in common cancers and their correlation with molecular cancer type. Cancer Epidemiol Biomarkers Prev 2014;23:2965–70.
21. Loi S, Sirtaine N, Piette F, Salgado R, Viale G, Van Eenoo F, et al. Prognostic and predictive value of tumor-infiltrating lymphocytes in a phase III randomized adjuvant breast cancer trial in node-positive breast cancer comparing the addition of docetaxel to doxorubicin with doxorubicin-based chemotherapy: BIG 02 to 98. J Clin Oncol 2013;31:860–7.
22. Fakih M, Sandhu J, Lim D, Li X, Li S, Wang C. Regorafenib, ipilimumab, and nivolumab for patients with microsatellite stable colorectal cancer and disease progression with prior chemotherapy: a phase 1 nonrandomized clinical trial. JAMA Oncol 2023;9:627–634.
23. Schmid S, Diem S, Li Q, Krapf M, Flatz L, Leschka S, et al. Organ-specific response to nivolumab in patients with non-small cell lung cancer (NSCLC). Cancer Immunol Immunother 2018;67:1825–32.
24. Shimizu T, Miyake M, Nishimura N, Inoue K, Fujii K, Iemura Y, et al. Organ-specific and mixed responses to pembrolizumab in patients with unresectable or metastatic urothelial carcinoma: a multicenter retrospective study. Cancers (Basel) 2022;14:1735.
25. Kerioui M, Desmée S, Mercier F, Lin A, Wu B, Jin JY, et al. Assessing the impact of organ-specific lesion dynamics on survival in patients with recurrent urothelial carcinoma treated with atezolizumab or chemotherapy. ESMO Open 2022;7:100346.
26. Yu S, Zhang S, Xu H, Yang G, Xu F, Yang L, et al. Organ-specific immune checkpoint inhibitor treatment in lung cancer: a systematic review and meta-analysis. BMJ Open 2023;13:e059457.
27. Fakih M, Wang C, Sandhu J, Ye J, Egelston C, Li X. Immunotherapy response in microsatellite stable metastatic colorectal cancer is influenced by site of metastases. Eur J Cancer 2024;196:113437.
28. Conway JW, Braden J, Wilmott JS, Scolyer RA, Long GV, Pires da Silva I. The effect of organ-specific tumor microenvironments on response patterns to immunotherapy. Front Immunol 2022;13:1030147.
29. Pao W, Ooi C-H, Birzele F, Ruefli-Brasse A, Cannarile MA, Reis B, et al. Tissue-specific immunoregulation: a call for better understanding of the [L8D2Q2M0]immunostat[R8D2Q2M1] in the context of cancer. Cancer Discov 2018;8:395–402.
30. Chen W, Hoffmann AD, Liu H, Liu X. Organotropism: new insights into molecular mechanisms of breast cancer metastasis. NPJ Precis Oncol 2018;2:4.
31. DeNardo DG, Brennan DJ, Rexhepaj E, Ruffell B, Shiao SL, Madden SF, et al. Leukocyte complexity predicts breast cancer survival and functionally regulates response to chemotherapy. Cancer Discov 2011;1:54–67.
32. Jackson HW, Fischer JR, Zanotelli VRT, Ali HR, Mechera R, Soysal SD, et al. The single-cell pathology landscape of breast cancer. Nature 2020;578:615–20.
33. Wagner J, Rapsomaniki MA, Chevrier S, Anzeneder T, Langwieder C, Dykgers A, et al. A single-cell atlas of the tumor and immune ecosystem of human breast cancer. Cell 2019;177:1330–45.e18.
34. Hussein MR, Hassan HI. Analysis of the mononuclear inflammatory cell infiltrate in the normal breast, benign proliferative breast disease, in situ and infiltrating ductal breast carcinomas: preliminary observations. J Clin Pathol 2006;59:972–7.
35. Hutchinson KE, Yost SE, Chang C-W, Johnson RM, Carr AR, McAdam PR, et al. Comprehensive profiling of poor-risk paired primary and recurrent triple-negative breast cancers reveals immune phenotype shifts. Clin Cancer Res 2020;26:657–68.
36. Szekely B, Bossuyt V, Li X, Wali VB, Patwardhan GA, Frederick C, et al. Immunological differences between primary and metastatic breast cancer. Ann Oncol 2018;29:2232–9.
37. Schreiber RD, Old LJ, Smyth MJ. Cancer immunoediting: integrating immunity's roles in cancer suppression and promotion. Science 2011;331: 1565–70.
38. Angelova M, Mlecnik B, Vasaturo A, Bindea G, Fredriksen T, Lafontaine L, et al. Evolution of metastases in space and time under immune selection. Cell 2018;175:751–65.e16.
39. Chen R, Goodison S, Sun Y. Molecular profiles of matched primary and metastatic tumor samples support a linear evolutionary model of breast cancer. Cancer Res 2020;80:170–4.
40. Molecular heterogeneity and evolution in breast cancer. Ann Rev Cancer Biol 2021;5:79–94.
41. Restle D, Dux J, Li X, Byun AJ, Choe JK, Li Y, et al. Organ-specific heterogeneity in tumor-infiltrating immune cells and cancer antigen expression in primary and autologous metastatic lung adenocarcinoma. J Immunother Cancer 2023;11:e006609.
42. Ye J, Guo W, Wang C, Egelston CA, D'Apuzzo M, Shankar G, et al. Peritumoral immune-suppressive mechanisms impede intratumoral lymphocyte infiltration into colorectal cancer liver versus lung metastases. Cancer Res Commun 2023;3:2082–95.
43. Conway JW, Rawson RV, Lo S, Ahmed T, Vergara IA, Gide TN, et al. Unveiling the tumor immune microenvironment of organ-specific melanoma metastatic sites. J Immunother Cancer 2022;10:e004884.
44. Christo SN, Evrard M, Park SL, Gandolfo LC, Burn TN, Fonseca R, et al. Discrete tissue microenvironments instruct diversity in resident memory T cell function and plasticity. Nat Immunol 2021;22:1140–51.
45. Connors TJ, Matsumoto R, Verma S, Szabo PA, Guyer R, Gray J, et al. Site-specific development and progressive maturation of human tissue-resident memory T cells over infancy and childhood. Immunity 2023;56: 1894–909.e5.
46. Shi F-D, Ljunggren H-G, La Cava A, Van Kaer L. Organ-specific features of natural killer cells. Nat Rev Immunol 2011;11:658–71.
47. Zhao J, Andreev I, Silva HM. Resident tissue macrophages: key coordinators of tissue homeostasis beyond immunity. Sci Immunol 2024;9:eadd1967.
48. Raz E. Organ-specific regulation of innate immunity. Nat Immunol 2007;8: 3–4.
49. Spranger S, Luke JJ, Bao R, Zha Y, Hernandez KM, Li Y, et al. Density of immunogenic antigens does not explain the presence or absence of the T-cell–inflamed tumor microenvironment in melanoma. Proc Natl Acad Sci U S A 2016;113:E7759–68.
50. Hildner K, Edelson BT, Purtha WE, Diamond M, Matsushita H, Kohyama M, et al. Batf3 deficiency reveals a critical role for CD8alpha+ dendritic cells in cytotoxic T cell immunity. Science 2008;322:1097–100.
51. Spranger S, Dai D, Horton B, Gajewski T. Tumor-residing Batf3 dendritic cells are required for effector T cell trafficking and adoptive T cell therapy. Cancer Cell 2017;31:711–23.e4.
52. Sung S-SJ, Fu SM, Rose CE, Gaskin F, Ju S-T, Beaty SR. A major lung CD103 (α_E)-β_7 integrin-positive epithelial dendritic cell population expressing langerin and tight junction proteins. J Immunol 2006;176:2161–72.
53. Bergenfelz C, Roxå A, Mehmeti M, Leandersson K, Larsson A-M. Clinical relevance of systemic monocytic-MDSCs in patients with metastatic breast cancer. Cancer Immunol Immunother 2020;69:435–48.
54. Bronte V, Brandau S, Chen S-H, Colombo MP, Frey AB, Greten TF, et al. Recommendations for myeloid-derived suppressor cell nomenclature and characterization standards. Nat Commun 2016;7:12150.
55. Yu J, Green MD, Li S, Sun Y, Journey SN, Choi JE, et al. Liver metastasis restrains immunotherapy efficacy via macrophage-mediated T cell elimination. Nat Med 2021;27:152–64.
56. Lee JC, Mehdizadeh S, Smith J, Young A, Mufazalov IA, Mowery CT, et al. Regulatory T cell control of systemic immunity and immunotherapy response in liver metastasis. Sci Immunol 2020;5:eaba0759.

57. Largillier R, Ferrero J-M, Doyen J, Barriere J, Namer M, Mari V, et al. Prognostic factors in 1,038 women with metastatic breast cancer. Ann Oncol 2008;19:2012–9.
58. Jaillon S, Ponzetta A, Di Mitri D, Santoni A, Bonecchi R, Mantovani A. Neutrophil diversity and plasticity in tumour progression and therapy. Nat Rev Cancer 2020;20:485–503.
59. Powell DR, Huttenlocher A. Neutrophils in the tumor microenvironment. Trends Immunol 2016;37:41–52.
60. McFarlane AJ, Fercoq F, Coffelt SB, Carlin LM. Neutrophil dynamics in the tumor microenvironment. J Clin Invest 2021;131:e143759.
61. Ayala de la Peña F, Yufera Soler J, Ivars MA, Fernandez Sanchez A, Navarro Manzano E, De la Morena Barrio P, et al. Neutrophil-lymphocyte ratio (NLR) as a prognostic factor in metastatic breast cancer. Ann Oncol 2017; 28(Suppl 5):v94.
62. Gungabeesoon J, Gort-Freitas NA, Kiss M, Bolli E, Messemaker M, Siwicki M, et al. A neutrophil response linked to tumor control in immunotherapy. Cell 2023;186:1448–64.e20.
63. Hirschhorn D, Budhu S, Kraehenbuehl L, Gigoux M, Schröder D, Chow A, et al. T cell immunotherapies engage neutrophils to eliminate tumor antigen escape variants. Cell 2023;186:1432–47.e17.
64. Riggio AI, Varley KE, Welm AL. The lingering mysteries of metastatic recurrence in breast cancer. Br J Cancer 2021;124:13–26.
65. Carpenter DJ, Granot T, Matsuoka N, Senda T, Kumar BV, Thome JJC, et al. Human immunology studies using organ donors: impact of clinical variations on immune parameters in tissues and circulation. Am J Transpl 2018;18: 74–88.
66. Geukens T, Maetens M, Hooper JE, Oesterreich S, Lee AV, Miller L, et al. Research autopsy programmes in oncology: shared experience from 14 centres across the world. J Pathol 2024;263:150–65.
67. Desmedt C, Carey LA. Global post-mortem tissue donation programmes to accelerate cancer research. Nat Rev Cancer 2024;24:289–90.
68. Geukens T, De Schepper M, Van Den Bogaert W, Van Baelen K, Maetens M, Pabba A, et al. Rapid autopsies to enhance metastatic research: the UPTIDER post-mortem tissue donation program. NPJ Breast Cancer 2024; 10:1–14.
69. De Mattos-Arruda L, Sammut SJ, Ross EM, Bashford-Rogers R, Greenstein E, et al. The genomic and immune landscapes of lethal metastatic breast cancer. Cell Rep 2019;28:2690–708.e1.
70. Wu AM, Pandit-Taskar N. ImmunoPET: harnessing antibodies for imaging immune cells. Mol Imaging Biol 2022;24:181–97.